



CrossMark
click for updates

Cite this: *RSC Adv.*, 2014, 4, 60386

Reduced graphene oxide–titania based platform for label-free biosensor†

Pratima R. Solanki,^{*ab} Saurabh Srivastava,^{bcd} Md. Azahar Ali,^b Rajesh Kr. Srivastava,^{ce} Anchal Srivastava^c and B. D. Malhotra^{*bd}

A label-free biosensor has been fabricated using a reduced graphene oxide (RGO) and anatase titania (ant-TiO₂) nanocomposite, electrophoretically deposited onto an indium tin oxide coated glass substrate. The RGO-ant-TiO₂ nanocomposite has been functionalized with protein (horseradish peroxidase) conjugated antibodies for the specific recognition and detection of *Vibrio cholerae*. The presence of Ab-Vc on the RGO-ant-TiO₂ nanocomposite has been confirmed using electron microscopy, Fourier transform infrared spectroscopy and electrochemical techniques. Electrochemical studies relating to the fabricated Ab-Vc/RGO-ant-TiO₂/ITO immunoelectrode have been conducted to investigate the binding kinetics. This immunosensor exhibits improved biosensing properties in the detection of *Vibrio cholerae*, with a sensitivity of $18.17 \times 10^6 \text{ F mol}^{-1} \text{ L}^{-1} \text{ m}^{-2}$ in the detection range of 0.12–5.4 nmol L⁻¹, and a low detection limit of 0.12 nmol L⁻¹. The association (k_a), dissociation (k_d) and equilibrium rate constants have been estimated to be 0.07 nM, 0.002 nM and 0.41 nM, respectively. This Ab-Vc/RGO-ant-TiO₂/ITO immunoelectrode could be a suitable platform for the development of compact diagnostic devices.

Received 26th August 2014
Accepted 21st October 2014

DOI: 10.1039/c4ra09265a

www.rsc.org/advances

1. Introduction

Recent advancements in nanoscience and nanotechnology have led to increased interest in the development of point-of-care diagnostic devices for global health, environmental monitoring and food safety.^{1–4} Multifunctional nanomaterials have been found to be promising candidates for the sensitive and selective detection of pathogens, smRNA, PNA, aptamers, *etc.*^{5,6} Carbon allotropes, like graphene oxide (GO), fullerenes, carbon nanotubes, *etc.*, have been explored for cellular imaging, tissue engineering, intercalation materials, drug delivery biomaterials and biosensors.^{7–11} For biosensor fabrication, the presence of available functional groups (*e.g.* hydroxyl, epoxide, carbonyl, carboxyl, *etc.*) on the basal planes/edges of a GO sheet may facilitate the conjugation of proteins or biomolecules.^{12–16} Due to its small size, intrinsic electrochemical properties, large

planar area, and useful non-covalent interactions with proteins, GO is an exciting material for biomedical applications.

The electrical conductivity of GO can be tuned *via* chemical reduction, resulting in the formation of reduced graphene oxide (RGO). Compared to GO, RGO provides enhanced electrochemical properties, excellent mobility of charge carriers, and can be easily functionalized with biomolecules^{14,15,17} due to its large surface area and high density of edge-plane-like defects that may allow fast heterogeneous electron transfer.¹⁸ In addition, ease of processing the material, low cost of synthesis and mechanical flexibility of RGO may lead to a wide range of applications, including biosensors,^{18–20} field effect transistors,²¹ photovoltaics²² and photodetectors.²³ GO modified electrochemically pre-anodized screen-printed carbon electrodes have been developed for the determination of nicotinamide adenine dinucleotide in a neutral aqueous solution.¹⁴ RGO has been utilized for the detection of aflatoxin B1 using an electrochemical technique.²⁴

The metal oxide nanoparticles (MOsN) based nanocomposites with carbonaceous materials, including RGO, have been found to display improved electronic properties that play a vital role in the fabrication of electrochemical biosensors.^{25–28} It has been reported that the use of MOsN and GO nanocomposites may result in improved biosensor efficacy compared to when a single component is used.^{29–33} Recently, a GO and titanium oxide (TiO₂) nanocomposite has been explored for the development of lithium ion batteries, photocatalysts and dye sensitized solar cells.³⁴ However, the RGO and MOsN

^{*}Special Centre for Nano Sciences, Jawaharlal Nehru University, New Delhi-110067, India. E-mail: pratimarsolanki@gmail.com

^bDepartment of Science and Technology Centre on Biomolecular Electronics, Biomedical Instrumentation Section, CSIR-National Physical Laboratory, Dr K. S. Krishnan Marg, New Delhi 110012, India. E-mail: bansi.malhotra@gmail.com; Fax: +91 11 45609312; Tel: +91 11 45609152

^cDepartment of Physics, Banaras Hindu University, Varanasi, 221005, India

^dDepartment of Biotechnology, Delhi Technical University, Shahbad Daultapur, Main Bawana Road, Delhi-110042, India

^eDepartment of Physics, Indian Institute of Science, Bangalore-560012, India

† Electronic supplementary information (ESI) available. See DOI: 10.1039/c4ra09265a

composite have not yet been used for the fabrication of an electrochemical immunosensor.

Anatase TiO₂ (ant-TiO₂) is an interesting material, due to its long-term stability, strong oxidizing power, low cost, biocompatibility and non-toxicity.³⁵ Moreover, TiO₂ nanoparticles have the ability to adsorb desired proteins and effectively coordinate the electron transfer between protein molecules and the electrode. Ali *et al.* have recently fabricated a microfluidic biochip using ant-TiO₂ nanoparticles for the detection of biomolecules. The high-purity single crystal with a high percentage of reactive (001) facets of ant-TiO₂ may cause improved catalytic behaviour and selectivity.³⁵ Keeping this in view, efforts have been made towards the fabrication of a RGO and ant-TiO₂ nanocomposite platform for the fabrication of an electrochemical immunosensor. The integration of ant-TiO₂ with RGO, using a direct self-assembly approach, may result in increased van der Waals interactions between the graphene basal plane and the oxygen moiety present on the ant-TiO₂ surface. A homogeneous distribution of ant-TiO₂ nanoparticles on multilayered RGO may lead to enhanced electrochemical behavior. Shen *et al.* have synthesized a nanocomposite of RGO and TiO₂ nanoparticles.³⁶ Yun *et al.* have synthesized a RGO-TiO₂ nanotube platform to improve the electron transfer kinetics.³⁷ Palanisamy *et al.* have fabricated a glucose sensor based on electrodeposition of ZnO microflowers on a RGO modified glassy carbon electrode.³⁸ The low isoelectric point (IEP ~ 4.0–5.0) of TiO₂ nanoparticles allows them to bind easily with biomolecules of high IEP, especially with horseradish peroxidase (HRP; IEP ~ 8.9). The TiO₂ nanoparticles are known to provide increased stability to HRP molecules. However, the direct binding of TiO₂ and HRP labeled antibodies *via* electrostatic interactions may provide a well oriented immune platform that could perhaps preserve structural integrity of the molecules. The favorable orientation of antibodies on the desired surface could be achieved *via* binding of proteins A and G³⁹ onto the HRP conjugated TiO₂ surface. Li *et al.* have deposited TiO₂ nanorods on a titanium electrode as a supporting matrix for the immobilization of nafion-coated HRP. They have illustrated that the strong electrostatic interactions between HRP and TiO₂ nanorods perhaps facilitate direct electron transfer between the electrode and biomolecules.⁴⁰

Vibrio cholerae (Vc) is a causative agent of diarrhea and acidosis in humans and is known to be highly lethal.⁴¹ Solanki *et al.* have fabricated a nickel oxide nanowire based immunosensor using protein A as a linker for the immobilization of anti-*Vibrio cholerae* antibodies.⁴¹ A chemiluminescent biosensor has been developed for cholera toxin detection using a supported lipid membrane as a sensing surface and the HRP/ganglioside GM1-functionalized liposome as a detection probe.⁴² A disposable amperometric immunosensor for *V. cholerae* has been fabricated using a screen-printed electrode of homemade carbon inks consisting of a mixture of polystyrene and graphite particles.⁴³ Chiriaco *et al.* have developed an electrochemical immunosensor based on mixed self-assembled monolayers of 11-mercaptopundecanoic acid and 2-mercaptoethanol on a gold electrode. This electrode can be used to detect cholera toxin from 1–100 ng mL⁻¹.⁴⁴ Thus, there is an increased demand for

the availability of a rapid, sensitive and reproducible analytical tool for the detection of *Vibrio cholerae* (Vc) concentration.

We report results of the studies relating to the fabrication of an electrochemical label-free immunosensor for the detection of *Vibrio cholerae*. The synthesized TiO₂-RGO composite is electrophoretically deposited onto an indium tin oxide (ITO) coated glass substrate for the immobilization of HRP conjugated antibodies specific to *Vibrio cholerae*. The HRP conjugated antibodies provide a well oriented sensing platform on the TiO₂-RGO nanocomposite, resulting in improved sensitivity and a wide detection range. To the best of our knowledge, this is the first time that a TiO₂-RGO composite has been used to develop an electrochemical immunosensor for the detection of *Vibrio cholerae*.

2. Experimental

2.1 Materials and reagents

All chemicals were purchased from Sigma Aldrich, USA. The protein (horseradish peroxidase; HRP) conjugated antibodies specific to *Vibrio cholerae* (Ab-Vc), bovine serum albumin (BSA) and *Vibrio cholerae* were obtained from M/s Genetix Biotech, Asia Pvt. Ltd, India. *N*-Ethyl-*N*-(3-dimethylaminopropyl) carbodiimide (EDC), *N*-hydroxysuccinimide (NHS) and graphite powder flakes (45 μm, >99.99 wt%) were procured from Sigma-Aldrich, USA.

2.2 Synthesis of GO

GO was synthesized using graphite powder flakes *via* an improved Hummer's method and purified accordingly to yield a brown powder, as described in our previous published work.²⁴ Briefly, 1.5 g of graphite powder was pre-oxidized by reacting it with a mixture of 40 mL of 98% H₂SO₄, 5 g K₂S₂O₈ and 5 g of P₂O₅ for 4 h at 80 °C. The obtained suspension was washed with deionized water 4–5 times and dried at 50 °C under vacuum. The pre-oxidized graphite was deoxidized by adding a mixture of concentrated H₂SO₄ : H₃PO₄ (180 : 13) with constant stirring. Then, 9 g of KMnO₄ was added to the mixture after 5 min, which was stirred continuously for 15 h at 50 °C. The reaction was stopped after about 15 h and the reactants were allowed to cool at room temperature, after which 200 mL of ice was poured into the mixture followed by 1.5 mL of H₂O₂ (30%). Then fine material was separated from the mixture using a U.S. standard testing sieve of pore size 30 mm and finally the filtration was performed. The supernatant was discarded and the filtrate was subjected to centrifugation at 5000 rpm for about 3 h. Multiple washing of the sediment material was performed several times with deionized water, 30% HCl and ethanol (100 mL of each) followed by centrifugation separation. The final sediment was suspended in 100 mL of ether and filtered through a PTFE membrane with a pore size of 0.45 μm. The semi-solid material obtained as graphene oxide (GO) was vacuum dried overnight. The solid brown powder of GO was thus obtained.

2.3 Reduction of GO

This powder, when dispersed in deionized water, yielded exfoliated sheets of GO upon sonication. The solution is stable over a period of two weeks, without any sign of aggregation. The reduction of GO was performed using the two-step reduction procedure reported in previous work.²⁴ On its dispersion in deionized water, the pH of the solution was increased to ~ 10 using 5 wt% sodium carbonate solution and sodium borohydride (NaBH_4) (400 mg) was directly added into the 200 mL GO suspension (1 mg mL^{-1}) under magnetic stirring and kept at 80°C for 1 h, resulting in a color change from brown to black. The solid product was then purified with water and ethanol washing, followed by drying and re-dispersion in H_2SO_4 at 120°C . This was then re-filtered through a $0.22 \mu\text{m}$ Dura pore membrane to yield RGO. The obtained RGO was partially reduced, such that it consisted of sufficient functional groups, controlled by the optimized NaBH_4 (52 mM) concentration. This chemically active RGO along with the functional groups showed good electrochemical properties. Thus, it could be highly valuable for composite formation and the attachment of antibodies for the development of an immunosensor for Vc detection.

2.4 Synthesis of ant-TiO₂ nanoparticles

Titanium(IV) butoxide was dissolved in 2-methoxy ethanol to prepare a 5 (wt%) precursor sol solution *via* the dropwise addition of H_2O and nitric acid under continuous stirring to obtain the hydroxide. The anatase titania (ant-TiO₂) was then prepared using a procedure reported earlier.⁴⁵

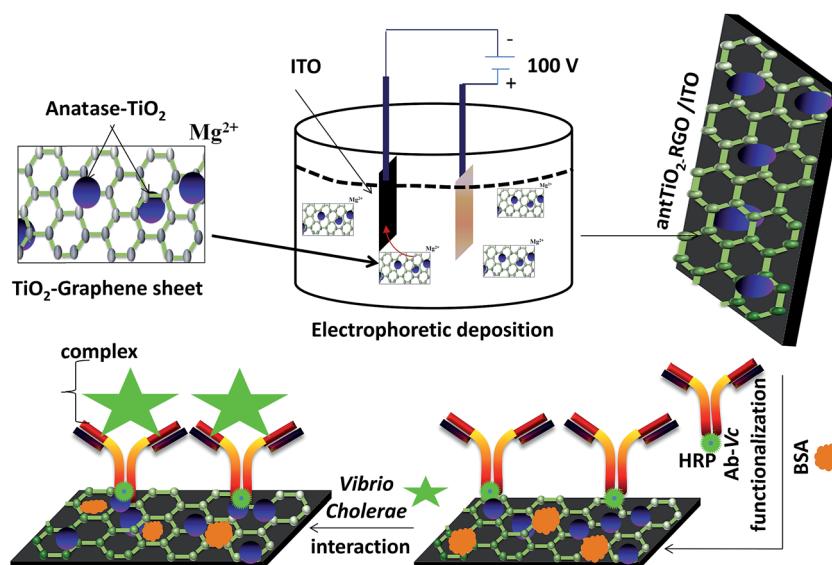
2.5 Biosensing platform

The RGO-ant-TiO₂ nanocomposite was fabricated on an ITO (0.25 cm^2) coated glass plate using the electrophoretic deposition (EPD) technique. The interaction between the ant-TiO₂ and RGO occurs electrostatically, due to the presence of a positive

charge and negative charge, respectively. A well dispersed stock solution (1 : 1) of RGO (50 mg dL^{-1}) and TiO₂ (50 mg dL^{-1}) in acetonitrile was prepared by ultrasonication (50 W, 0.25 A) for about 3 h at room temperature (25°C). For the fabrication of the RGO-ant-TiO₂ nanocomposite, 100 μL of each stock solution was dispersed in 10 mL of acetonitrile to make a colloidal suspension of RGO and TiO₂. Electrophoretic deposition was performed in a two-electrode cell by applying a DC voltage (100 V) for about 2 min. To obtain enhanced deposition, 10^{-5} to 10^{-4} mol of $\text{Mg}(\text{NO}_3)_2 \cdot 6\text{H}_2\text{O}$ was added into the suspension, which acted as the electrolyte for EPD that provided a net positive charge for the mixture of RGO-ant-TiO₂ enhanced deposition onto the anode surface that was ITO. A platinum foil ($1 \text{ cm} \times 2 \text{ cm}$) was used as the cathode and a pre-cleaned ITO-coated glass substrate with a sheet resistance of $30 \Omega \text{ cm}^{-1}$ as the anode. These two electrodes, separated by 1 cm and placed parallel to each other, were dipped in the colloidal suspension of RGO-ant-TiO₂. The RGO-ant-TiO₂/ITO electrodes were removed from the suspension followed by washing with deionised water and drying.

The zeta potential measurement for the RGO-ant-TiO₂ composite revealed that this composite shows a net positive charge of +16.8 mV in an acetonitrile solvent. Thus, during electrophoretic deposition, the dispersed RGO-ant-TiO₂ composite was deposited uniformly on the ITO surface under the application of a negative potential.

Prior to the covalent immobilization of antibodies (Ab-VC), the COOH group of the RGO/ITO electrode was activated using EDC as the coupling agent and NHS as the activator (Scheme 1). 1 ng mL^{-1} anti-AFB1 antibody solution was freshly prepared in phosphate buffer (PBS, pH 7.4). Ten microliters of this solution was uniformly spread on the EDC/NHS activated RGO-ant-TiO₂/ITO electrode surface, which was then incubated in a humid chamber for about 4 h at room temperature. The covalent interaction could form a strong amide (CO-NH) bond between



Scheme 1 Fabrication of the immunosensor for *Vibrio cholerae* detection.

the carboxyl group of RGO and the amine group of HRP conjugated Ab-Vc. Moreover, the HRP can be facilitated this interaction, due to its natural electrostatic interactions with ant-TiO₂ nanoparticles and RGO. This immunoelectrode was rinsed with phosphate buffer (PB; pH 7.0) to remove any unbound Ab-Vc. Finally, the Ab-Vc/RGO-ant-TiO₂/ITO immunoelectrode was treated with BSA (1 mg mL⁻¹) solution for about 4 h to block non-specific sites (Scheme 1). The BSA/Ab-Vc/RGO-ant-TiO₂/ITO immunoelectrode was stored at 4 °C when not in use.

2.6 Instrumentation

The fabricated RGO-ant-TiO₂/ITO electrode and BSA/Ab-Vc/RGO-ant-TiO₂/ITO immunoelectrode were characterized using Fourier transform infrared spectrometry (FT-IR, PerkinElmer, and Spectrum BX II). An X-ray diffraction (XRD) pattern of the RGO-ant-TiO₂ film was obtained using a RigakuD/Max 2200 diffractometer with CuK_α radiation at $\lambda = 1.5406 \text{ \AA}$ and Raman spectroscopy (HR800 LabRam, Horiba/Jobin-Yvon) was performed. Transmission electron microscopy (TEM, Tecnai-G2F30STWINT), scanning electron microscopy (SEM LEO 440) and atomic force microscopy (AFM, Park Systems XE70) were used to investigate the structural and morphological properties of RGO-ant-TiO₂ and BSA/Ab-Vc/RGO-ant-TiO₂. The electrochemical analysis was conducted using an Autolab Potentiostat/Galvanostat with a three-electrode system consisting of a working electrode, platinum wire as the auxiliary electrode, and Ag/AgCl acting as the reference electrode in phosphate buffer saline (PBS, pH 7.0, 0.9% NaCl) containing 5 mM [Fe(CN)₆]^{3-/4-} as the redox probe.

3. Results and discussion

3.1 X-ray diffraction studies

Fig. 1 shows the XRD patterns of RGO (a) and RGO-ant-TiO₂ (b). The broad and dominating peak seen at 24° (3.43 Å)

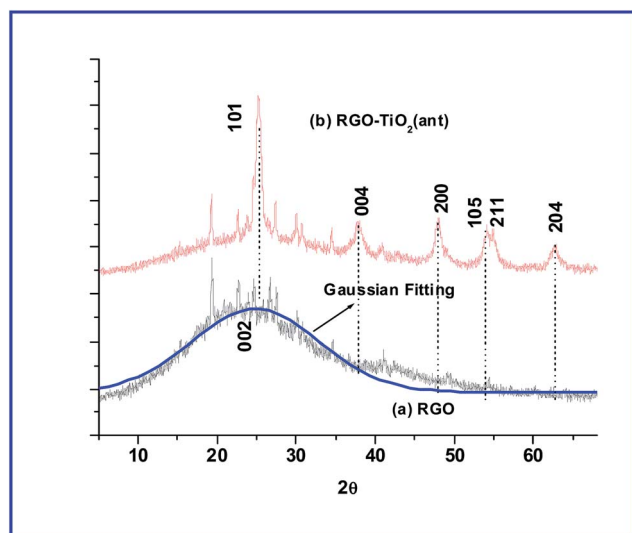


Fig. 1 Powder X-ray diffraction patterns of RGO (a) and RGO-ant-TiO₂ (b).

corresponds to the (002) reflection plane, indicating the reduction of GO due to the removal of the intercalated water molecules and the oxide groups of GO that allow the RGO sheets to pack tighter (smaller interlayer distance between sheets).³⁶ The RGO-ant-TiO₂ nanohybrid shows a prominent peak at 2θ : 25° and 48°, corresponding to diffraction from the (101) and (200) planes, indicating the anatase phase of TiO₂. The other diffraction planes observed for (004), (105), (211) and (204) (JCPDS 894921) reveal the presence of the anatase phase in TiO₂. The TiO₂ nanoparticles show all the peaks relating to ant-TiO₂ (ESI S1†). However, in the RGO-ant-TiO₂ composite, the diffraction plane (200) shows a weak peak corresponding to (101), indicating that the observed RGO layers are separated by nanoparticles acting as spacers and are not stacked together.⁴⁶ The average crystallite size of the ant-TiO₂ nanoparticles is estimated to be about 12 nm based on Scherrer's equation. No clear diffraction peak pertaining to graphite is observed, suggesting that the graphene sheet has a disordered structure.

3.2 Transmission electron microscopy (TEM) studies

Fig. 2A and B show results of the TEM studies conducted for the synthesized nanostructured TiO₂ and RGO-ant-TiO₂ hybrid. The colloidal solutions of TiO₂ and RGO-ant-TiO₂ composite were prepared on a carbon-coated copper grid using the electrophoretic technique. Image (A) shows the anatase TiO₂ nanoparticles, which are uniformly distributed. Some of the nanoparticles are agglomerated due to the surface charge of the nanoparticles. The average size of the TiO₂ nanoparticles varies from 10 to 15 nm and is in agreement with the results of the XRD studies. It appears that the RGO has a crumpled layered structure with several stacked layers of monoatomic graphene sheets (image B). The TEM image shows the edges of the graphene sheets with spherical TiO₂ nanoparticles attached on its surface, indicating the anchoring of TiO₂ nanoparticles on the graphene sheets. At the edges of the graphene sheet, the TiO₂ nanoparticles agglomerate may be due to the presence of surface charge.

3.3 Scanning electron microscopy studies

Fig. 2C and D show results of the scanning electron microscopy studies before and after the immobilization of the antibodies on the RGO-ant-TiO₂ composite. The image C shows that titania nanoparticles wrapped in graphene nanosheets can be seen on larger graphene flakes (highlighted by the red circle). In addition, some of these sheets are folded at the edges and in some regions wrinkles can be clearly seen. While, after antibody attachment (image D), a fine thread-like structure appears all over the RGO flakes, indicating the presence of the antibody molecules (immobilized antibody molecules are highlighted by the yellow dashed arrows and circle). Image D shows a smooth surface, indicating that the RGO-ant-TiO₂ nanohybrid surface is covered by the immobilized antibodies and BSA *via* π - π interactions.

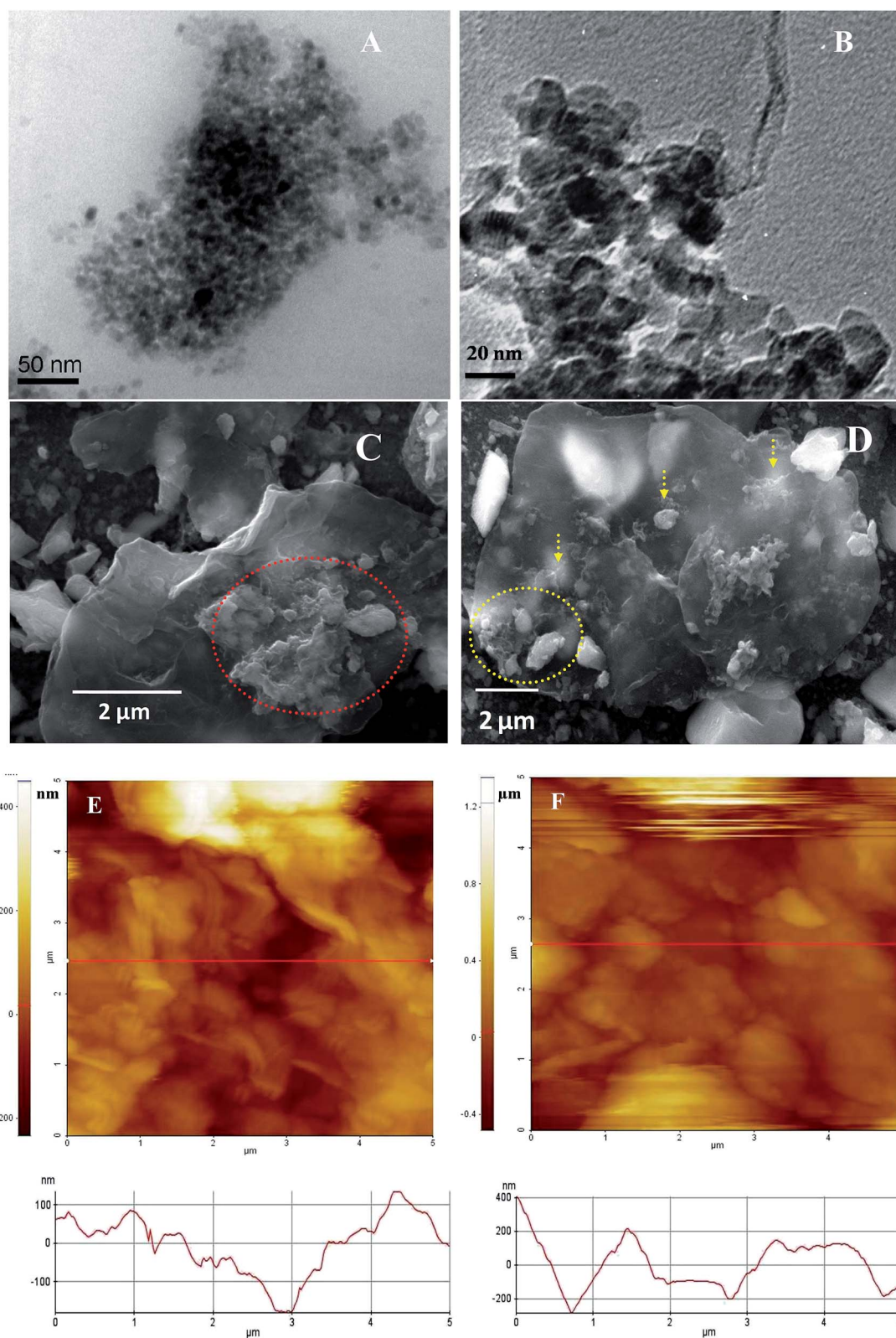


Fig. 2 (A) TEM image of TiO₂ nanoparticles and (B) the RGO-ant-TiO₂ composite; (C) and (D) show SEM images of the RGO-ant-TiO₂ composite and BSA/Ab-Vc/RGO-ant-TiO₂/ITO bioelectrode, respectively. (E) and (F) show AFM images of the RGO/ITO electrode and RGO-ant-TiO₂/ITO, respectively.

3.4 Atomic force microscopy studies

Fig. 2E and F show the two-dimensional atomic force microscopy (AFM) image of bare RGO film. Micron sized RGO flakes are distributed on the ITO substrate. The height distribution profile is shown below the image E. Some of the RGO sheets are attached to each other due to π - π stacking, resulting in a bigger size of sheets. After TiO₂ functionalization, the roughness of the RGO film is increased (image F) to 0.137 microns compared to that of the bare RGO (roughness: 76.4 nm). The TiO₂ nanoparticles are attached to RGO sheets on the basal plane as well as their edges during their deposition on ITO, which enhances the roughness of the film.

3.5 Raman spectroscopy studies

Raman spectroscopy studies were carried out to confirm the synthesis of RGO and the RGO-ant-TiO₂ nanohybrid (Fig. 3A). The inset shows an absorption peak at 1348 cm⁻¹ indicating that a D band arises due to the vibration of carbon atoms with the sp³ electronic configuration of disordered graphene. The peak at 1589 cm⁻¹ pertaining to the G band is associated with in-plane vibration of the sp²-bonded carbon atoms. The Raman spectrum of RGO-ant-TiO₂ shows peaks in the low frequency region pertaining to the B1g (399 cm⁻¹), A1g (513 cm⁻¹) and Eg (637 cm⁻¹) modes of the anatase phase. The intensity of the D band (1348 cm⁻¹) is found to be decreased compared to that of RGO (inset), and the wavenumber is shifted slightly lower, indicating the formation of the RGO-ant-TiO₂ nanohybrid. The intensity ratio of D/G of RGO-ant-TiO₂ is found to be low (0.95) compared to that of RGO (1.28), due to the increased average size of the sp² domain and defects in RGO. In case of the GO sheet, a decreased D/G intensity ratio is observed, suggesting that the defects in the graphene sheet increase after the reduction of GO.

3.6 Fourier transform infrared spectroscopy and UV-Vis studies

The FT-IR spectra of the RGO-ant-TiO₂/ITO film show the absorption peak at 579 cm⁻¹ (Ti-O bond) (ESI, Fig. S2†). The peak seen at 961 cm⁻¹ corresponds to the C-H stretching

vibration on the nanocomposite surface. Absorption peaks at 1052 cm⁻¹ and 1225 cm⁻¹ (C-O stretching vibration), as well as 1664 cm⁻¹ (C=C aromatic) and 1746 cm⁻¹ (C=O stretching vibration of COOH groups) indicate the presence of GO sheets in the RGO-ant-TiO₂/ITO film. The intense peak found near 1600 cm⁻¹ arises due to vibrations from the un-oxidized graphitic domains. The intensity of the absorption peak at 1600 cm⁻¹ increases due to amide bond formation after the immobilization of Ab-Vc and BSA (curve b). The peak shift in the fingerprint region (500-600 cm⁻¹) arises due to the incorporation of Ab-Vc followed by BSA onto the RGO-ant-TiO₂/ITO nanohybrid's surface. The additional peaks seen at 1047 cm⁻¹, 2030 cm⁻¹ and 3200 cm⁻¹ (curve b) reveal surface functionalization with Ab-Vc and BSA.

UV-Vis studies were conducted on the ant-TiO₂ (i), RGO-ant-TiO₂ (ii) and Ab-Vc/RGO-ant-TiO₂ (iii) electrodes in the wavelength range of 200 to 700 nm (ESI, Fig. S3†). The absorption peak found at 265 nm is due to the quantum confinement effect of the ant-TiO₂. The direct band gap was determined, by the $(\alpha h\nu)^2$ versus band energy plot (Fig. 3(ii)), using the Tauc equation

$$(\alpha h\nu)^2 = k(h\nu - E_g) \quad (1)$$

where α is the absorbance, h is the Planck constant and k is a constant. The direct band gap (E_g) of ant-TiO₂ (Fig. 3B, (a)) was estimated to be 3.8 eV, which is higher than that of the bulk material. It can be seen that distinct peaks appear at 334 nm and 250 nm, corresponding to the π - π^* transition of aromatic C-C bonds of RGO modified with ant-TiO₂. The band gap of the ant-TiO₂ electrode decreases to 2.55 eV, due to the incorporation of RGO (curve (b)). The intensity of the peak is found to be enhanced after the conjugation of antibodies with RGO-ant-TiO₂, indicating binding of the antibodies onto the nanocomposite surface. The band gap of Ab-Vc/RGO-ant-TiO₂ was found to be 2.68 eV (curve (c)).

3.7 Cyclic voltammetry studies

The cyclic voltammetry (CV) studies of the bare ITO electrode (a), RGO-ant-TiO₂/ITO nanohybrid (b), Ab-Vc/RGO-ant-TiO₂/

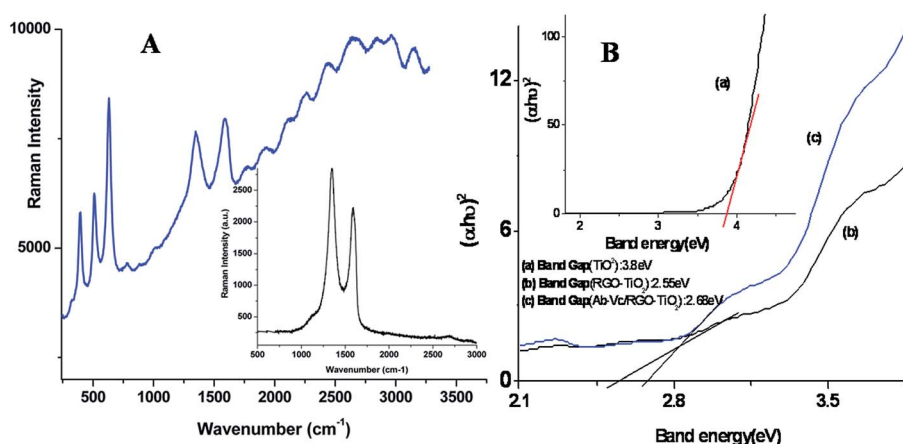


Fig. 3 (A) Raman spectra of the RGO-ant-TiO₂ nanohybrid and Raman spectra of RGO (inset) and (B) the plot of $(\alpha h\nu)^2$ versus the band energy (eV).

ITO immunoelectrode (c) and BSA/Ab-Vc/RGO-ant-TiO₂/ITO immunoelectrode (d) were performed in PBS containing 5 mM [Fe(CN)₆]^{3-/4-} at a scan rate of 20 mV s⁻¹ (ESI, Fig. S4†). It can be seen that the magnitude of the current of the RGO-ant-TiO₂/ITO electrode increases by about 4-fold (4.44 μA; curve b) and the oxidation current shifts toward a higher potential compared to that of the bare ITO (1.46 μA; curve a), due to fast electron transfer between the electrode and electrolyte. This may be attributed to the heterogeneous electron transfer in the graphene sheet and oxygen-containing groups at the edges of the graphene sheets. Besides this, the excellent electrocatalytic ant-TiO₂ embedded in the RGO results in faster electron transfer between the electrode and electrolyte. The RGO-ant-TiO₂/ITO electrode was functionalized with macromolecular protein-conjugated Ab-Vc, leading to a decreased flow of electrons, resulting in a reduced current (4.09 μA; curve c) with a slight shift towards a lower potential due to the insulating nature of protein molecules (HRP labeled Ab-Vc). The modification of the Ab-Vc/RGO-ant-TiO₂/ITO electrode with the insulating BSA (used as a blocking agent for the non-binding sites) results in hindered electron transfer between the medium and electrode, leading to a decrease in the magnitude of the current.

The cyclic voltammetric studies of the RGO-ant-TiO₂/ITO nanohybrid and BSA/Ab-Vc/RGO-ant-TiO₂/ITO immunoelectrode were carried out as a function of the scan rate (10–100 mV s⁻¹) (Fig. 4(A)). It was observed that the magnitude of the redox current proportionally increases (*I*_a is the anodic current) with respect to the square root of the scan rate, indicating a diffusion-controlled system (inset: Fig. 4A). The variation of the current for the different electrodes follows in eqn (2)–(5).

$$I_{pa}(A)_{\text{RGO-ant-TiO}_2 \text{ nanohybrid}} = 3.38 \times 10^{-6} A + 6.57 \times 10^{-5} A (s V^{-1}) \times \text{scan rate} (V s^{-1}) \text{ with } R^2 = 0.989... \quad (2)$$

$$I_{pc}(A)_{\text{RGO-ant-TiO}_2 \text{ nanohybrid}} = -3.34 \times 10^{-6} A - 4.14 \times 10^{-5} A (s V^{-1}) \times \text{scan rate} (V s^{-1}) \text{ with } R^2 = 0.99... \quad (3)$$

$$I_{pa}(A)_{\text{BSA/Ab-Vc/RGO-ant-TiO}_2 \text{ immunoelectrode}} = 1.42 \times 10^{-6} A + 3.62 \times 10^{-5} A (s V^{-1}) \times \text{scan rate} (V s^{-1}) \text{ with } R^2 = 0.99... \quad (4)$$

$$I_{pc}(A)_{\text{BSA/Ab-Vc/RGO-ant-TiO}_2 \text{ immunoelectrode}} = -1.31 \times 10^{-6} A - 1.02 \times 10^{-5} A (s V^{-1}) \times \text{scan rate} (V s^{-1}) \text{ with } R^2 = 0.965... \quad (5)$$

The surface concentrations of the RGO-ant-TiO₂/ITO nanohybrid and BSA/Ab-Vc/RGO-ant-TiO₂/ITO immunoelectrode were estimated from the plot of current versus potential (CV), using the equation: $I_p = \frac{n^2 F^2 I^* A V}{4RT}$ (Brown-Anson model), where *n* is the number of electrons transferred, *F* is the Faraday constant (96 584 C mol⁻¹), *I*^{*} is the surface concentration (mol m⁻²), *A* is the surface area of the electrode (0.25 × 10⁻⁴ m²), *V* is the scan rate (0.02 V s⁻¹), *R* is the gas constant (8.314 J (mol⁻¹ K⁻¹)), and *T* is the absolute temperature (298 K). The surface concentrations for the RGO-ant-TiO₂/ITO nanohybrid and BSA/Ab-Vc/RGO-ant-TiO₂/ITO immunoelectrode were found to be 23.7 and 15.4 mol

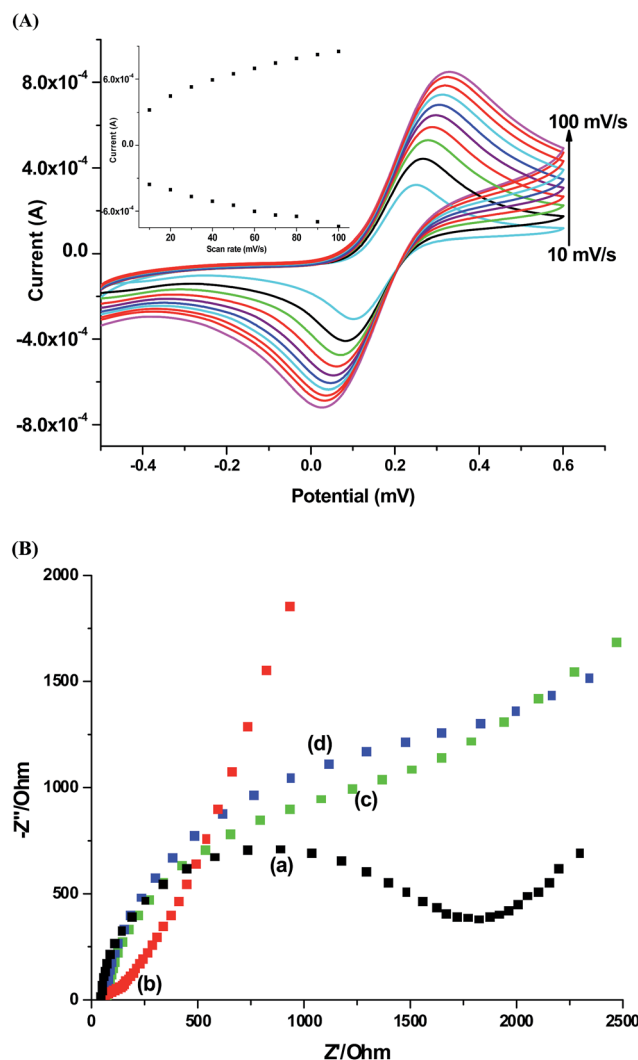


Fig. 4 (A) CV spectra of the RGO-ant-TiO₂/ITO nanohybrid at different scan rates varying from 10–100 mV s⁻¹. (B) EIS of the bare ITO electrode (a), RGO-ant-TiO₂/ITO nanohybrid (b), Ab-Vc/RGO-ant-TiO₂/ITO immunoelectrode (c) and BSA/Ab-Vc/RGO-ant-TiO₂/ITO bioelectrode (d).

m⁻², respectively. The change in surface concentration reveals the immobilization of antibodies on the RGO-ant-TiO₂/ITO electrode.

3.8 Impedance studies

Electrochemical impedance spectroscopy (EIS) involves the application of a sinusoidal ac potential, $E_t = E_0 \sin(\omega t)$ and $\omega = \pi f$ with dc offset potential.⁴⁷ In a linear system, the response signal (*I*_t), is shifted in phase (ϕ) and has a different amplitude, *I*₀, where $I_t = I_0 \sin(\omega t + \phi)$. Fourier transform of the voltage and current ratio gives the impedance response over a frequency range, given by eqn (6)

$$Z = \frac{E_t}{I_t} \quad (6)$$

The constant phase element (CPE) represents the capacitance between the electrode and electrolyte and its impedance value is given by the following equation;

$$Z_{\text{CPE}} = \frac{1}{Y_0(j\omega)^\alpha}; \alpha = \frac{\phi}{90} \quad (7)$$

where Y_0 represents the capacitance and $j = \sqrt{-1}$. The average capacitance for the CPE Helmholtz (a) and CPE Randles (b) equivalent circuits (ESI; Scheme A†) are given by Barsoukov *et al.*, 2005,⁴⁸ as in eqn (8) and (9), respectively. The magnitude of the capacitance can be estimated using the equivalent circuit model by fitting it to the experimental data.

$$C = \sqrt[\alpha]{\frac{Y_0}{R_{\text{soln}}^{-1}}} \quad (8)$$

$$C = \sqrt[\alpha]{\frac{Y_0}{R_{\text{immunoelctrode}}^{-1} + R_{\text{soln}}^{-1}}} \quad (9)$$

The CPE values of the RGO-ant-TiO₂/ITO nanohybrid (a), Ab-Vc/RGO-ant-TiO₂/ITO immunoelectrode (b) and BSA/Ab-Vc/RGO-ant-TiO₂/ITO immunoelectrode (c) were found to be 1.72×10^{-6} F, 0.67×10^{-6} F and 0.28×10^{-6} F, respectively (Fig. 4B). It was observed that the CPE decreases after the incorporation of Ab-Vc and BSA onto the RGO-ant-TiO₂/ITO nanohybrid-based electrode. This is perhaps due to the increased double layer distance between the BSA/Ab-Vc/RGO-ant-TiO₂/ITO immunoelectrode and electrolyte.

The semicircle diameter obtained from the EIS spectra from the Randles equivalent circuit is the charge transfer resistance (R_p). The charge transfer resistance controls the electron transfer kinetics of the redox-probe at the electrode/electrolyte interface. The change in the R_p value due to the addition of different substances adsorbed onto the electrode surface indicates surface modification. In this context, the Nyquist plots of the Randles equivalent circuit, *i.e.* Z_{im} as a function of Z_{re} , with a frequency range of 0.01–10⁵ Hz was obtained for the bare ITO electrode (a), RGO-ant-TiO₂/ITO nanohybrid (b), Ab-Vc/RGO-ant-TiO₂/ITO immunoelectrode (c) and BSA/Ab-Vc/RGO-ant-TiO₂/ITO immunoelectrode (d) (Fig. 4B). The linear fit of the RGO-ant-TiO₂/ITO electrode exhibits a nearly straight line, as a result of increased diffusion compared to that of the bare ITO (curve a). This may be due to the presence of an increased concentration of defects in the RGO-ant-TiO₂ nanohybrid that perhaps inhibits the direct electron flow from the redox probe [Fe(CN)₆]^{3-/4-} to the electrode surface. However, after the immobilization of Ab-Vc and BSA on the RGO-ant-TiO₂/ITO surface, the diffusion of electrons between the electrode and the redox ions decreases, resulting in an increase in the R_p value (2.28 kΩ, 2.89 kΩ; curve c & d). This may be attributed to the presence of bulky protein molecules that provide steric hindrance. In addition, the electrostatic interactions between the Ab-Vc and BSA and redox ions, or a change in the electronic properties of the RGO-ant-TiO₂/ITO nanohybrid may result in the reduced value of R_p . However, the increased value of R_p indicates the superior electrochemical activity of the Ab-Vc/

RGO-ant-TiO₂/ITO immunoelectrode. The relative change in R_p for the Ab-Vc/RGO-ant-TiO₂/ITO immunoelectrode is given in eqn (10). R_p^0 is the charge transfer after the interaction of CT with the Ab-Vc/RGO-ant-TiO₂/ITO immunoelectrode.

$$\Delta R_p = \frac{(R_p - R_p^0)}{R_p^0} \quad (10)$$

Table 1 shows the values of the impedance obtained for the different circuit elements used in modeling the sensor.

3.9 Electrochemical response studies

The impedimetric response of the BSA/Ab-Vc/RGO-ant-TiO₂/ITO immunoelectrode was measured as a function of the *Vibrio cholerae* concentration varying from 10 to 450 ng mL⁻¹ in PBS containing [Fe(CN)₆]^{3-/4-} with an incubation time of about five minutes (Fig. 5A). It was found that the capacitance decreases with an increasing Vc concentration. This may perhaps be assigned to the antibody-antigen (Ab-Ag) interaction leading to a change in the dielectric/blocking properties of the electrolyte-electrode interface.^{49,50} The capacitance value between the RGO-ant-TiO₂ based immunoelectrode and the electrolyte is $\frac{\epsilon\epsilon_0 A}{d}$, where ϵ_0 (F m⁻¹) is the permittivity of free space, ϵ is the relative dielectric constant, A (m²) is the surface area and d (m) is the distance. The decrease of the measured capacitance due to the increase of the distance between the electrode and electrolyte is thus expected, due to the interaction of Vc with the Ab-Vc. In addition, the interaction between the Ab-Vc and Vc causes a decrease in the magnitude of the capacitance, since fewer polar Vc protein molecules replace the water molecules on the electrode surface. The capacitive immunosensor can be calibrated by plotting the change in the capacitance *versus* the analyte (antigen) concentration. This calibration curve exhibits a linear fit as $C_{\text{dl}} \text{ (F)} = 0.64 \times 10^{-6} \text{ (F)} + 4.52 \times 10^2 \text{ F mol}^{-1} \text{ L}^{-1} \times \{\text{Vc concentration}\}$. A linear relationship is observed in the range of 10–450 ng mL⁻¹ (0.12–5.4 nmol L⁻¹). The change in the capacitance value of the BSA/Ab-Vc/RGO-ant-TiO₂/ITO immunoelectrode was monitored as a function of the Vc concentration under similar conditions (Fig. 5A). It was found that the R_p value increases with an increasing Vc concentration on the BSA/Ab-Vc/RGO-ant-TiO₂/ITO immunoelectrode (Fig. 5B). This is due to the antigen-antibody complex formation of Vc at the electrode surface. The increased R_p value indicates that the insulating layer on the BSA/Ab-Vc/RGO-ant-TiO₂/ITO immunoelectrode surface inhibits the penetration of the redox species to the electrode surface, resulting in the higher

Table 1 Equivalent circuit elements of the different fabricated electrodes

Electrodes	R_s (Ω)	R_{CT} (kΩ)	C_{dl} (μF)	n
RGO-ant-TiO ₂ /ITO	-1.6×10^3	1.66	0.017	0.25
Ab-Vc/RGO-ant-TiO ₂ /ITO	7.06×10^1	2.28	0.668	0.89
BSA/Ab-Vc/RGO-ant-TiO ₂ /ITO	4.79×10^1	2.89	0.289	0.84

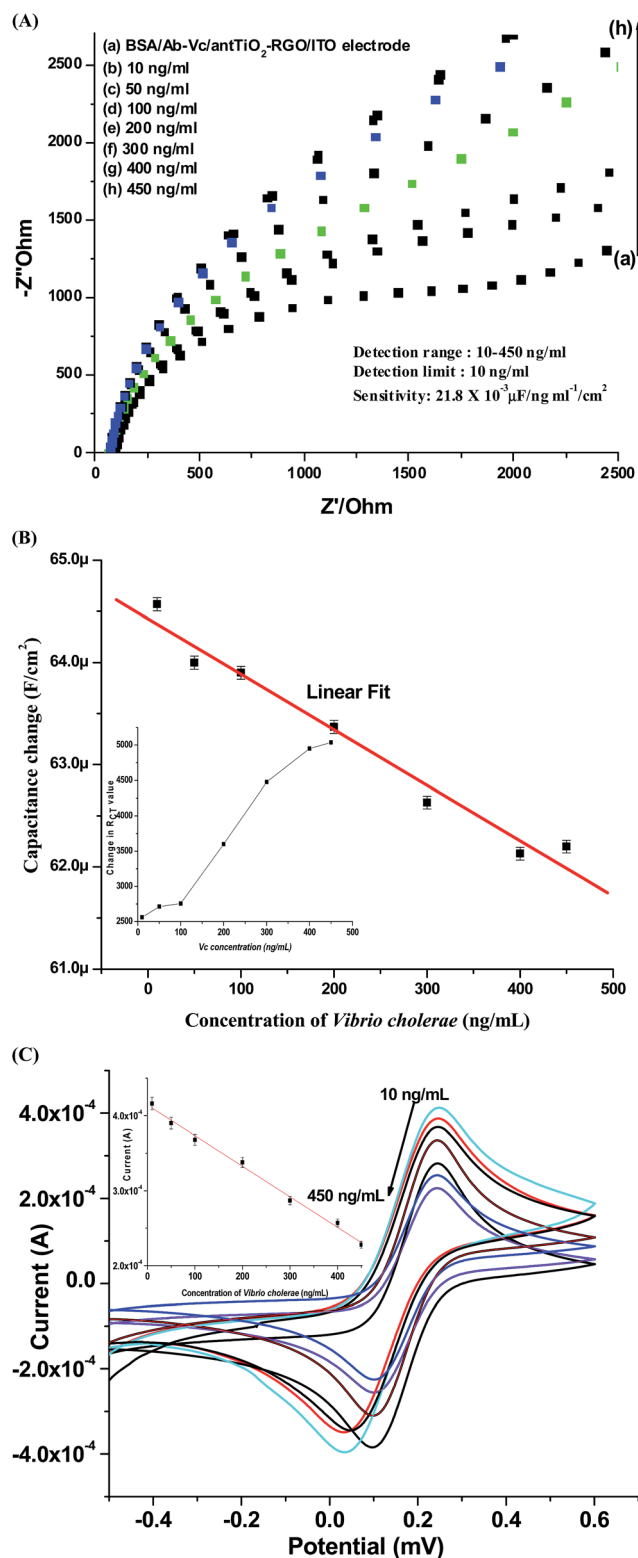


Fig. 5 (A) Electrochemical impedance response studies of the BSA/Ab-Vc/RGO-ant-TiO₂/ITO immunoelectrode as a function of the *Vibrio cholerae* concentration (10–450 ng mL⁻¹). (B) Calibration plot of the capacitance of the BSA/Ab-Vc/RGO-ant-TiO₂/ITO immunoelectrode against the *Vibrio cholerae* concentration (inset: calibration plot of the charge transfer resistance (R_{ct}) of the BSA/Ab-Vc/RGO-ant-TiO₂/ITO immunoelectrode against the *Vibrio cholerae* concentration). (C) The response studies of the BSA/Ab-Vc/RGO-ant-TiO₂/ITO immunoelectrode as a function of the *Vibrio cholerae*

diameter of the EIS spectra. A linear relationship was observed between the value of the capacitance of the BSA/Ab-Vc/RGO-ant-TiO₂/ITO immunoelectrode and Vc concentration (Fig. 5A). The charge transfer resistance (R_{ct}) of the BSA/Ab-Vc/RGO-ant-TiO₂/ITO immunoelectrode was found to increase with increasing concentrations of Vc (inset, Fig. 5B). Treatment with 0.2 M glycine solution of pH 2.4 for about two minutes resulted in 95% regeneration of the immunoelectrode.

The kinetics of this immunosensor was investigated using EIS at room temperature (298 K). The reaction equation for the binding between the antigen and antibodies was calculated as $[A] + [B] \leftrightarrow [AB]$. The rate of the formation of the antigen and antibody complex as the association phase is given in eqn (11);

$$\frac{d[AB]}{dt} = k_a[A][B] - k_d[AB] \quad (11)$$

where k_a and k_d are the association and dissociation rate constants, respectively. The association and dissociation rate constants for Ab-Vc binding are estimated to be 5.845 ng mL⁻¹ (0.07 nM) and 0.171 ng mL⁻¹ (0.002 nM), respectively. The equilibrium constant for association ($K_A = k_a/k_d$) is found to be 34.18 ng mL⁻¹ (0.41 nM). These results indicate the strong binding affinity of the BSA/Ab-Vc/RGO-ant-TiO₂/ITO immunoelectrode for a *Vibrio cholerae* moiety. The change in the electrochemical response of the BSA/Ab-Vc/RGO-ant-TiO₂/ITO immunoelectrode as a function of the *Vibrio cholerae* concentration (10–450 ng mL⁻¹) was investigated using CV under similar conditions. The magnitude of the peak current decreases as the concentration of *Vibrio cholerae* increases (Fig. 5C). This may be due to antigen-antibody interactions on the transducer surface, which block the charge transfer from the electrolyte to the electrode. The transfer of electrons from the [Fe(CN)₆]^{3-/4-} redox reaction may be blocked due to the formation of highly organized layers on the electrode surface, because these redox species do not penetrate the layer and reach the conductive electrode surface. With the addition of the Vc moieties to the BSA/Ab-Vc/RGO-ant-TiO₂/ITO immunoelectrode, these Vc protein molecules form an insulating layer on the electrode, resulting in the increased diameter of the semi-circle, implying higher charge transfer resistance. Across the detection range of 10–450 ng mL⁻¹, a sensitivity of 1.6 μA ng⁻¹ mL⁻¹ cm⁻² and linear regression coefficient (r^2) of 0.99 were obtained. The electrochemical response study was conducted without incorporating TiO₂ nanoparticles onto the RGO bioelectrode, and as a function of the Vc concentration (Fig. S5†). A sensitivity of 0.22 μA ng⁻¹ mL⁻¹ with r^2 of 0.92 were obtained, in the detection range of 100–300 ng mL⁻¹, which are less than those of the BSA/Ab-Vc/RGO-ant-TiO₂/ITO immunoelectrode.

The BSA/Ab-Vc/RGO-ant-TiO₂/ITO immunosensor yields a high sensitivity 21.8 × 10⁻³ μF ng⁻¹ mL⁻¹ cm⁻² (18.17 × 10⁶ F mol⁻¹ L⁻¹ m⁻²), with a standard deviation of 2.556 and a linear regression coefficient (r^2) of 0.986. The higher sensitivity of this fabricated biosensor may be due to the functional properties

concentration. The inset shows the plot of the current value versus the *Vibrio cholerae* concentration.

and larger surface area of the RGO-ant-TiO₂ nanohybrid. The presence of available functional groups on the RGO-ant-TiO₂ may increase the loading capacity for antibody molecules, resulting in improved biosensor efficacy. This immunosensor shows a lower detection value of 0.148 ng mL⁻¹ (0.0018 nmol L⁻¹), calculated using the $3\sigma_b/m$ criteria, where m is the slope of the calibration graph and σ_b is the standard deviation of the blank signal. The wide detection range of *Vc* was found to be 10–450 ng mL⁻¹ or 0.12–5.4 nmol L⁻¹. Solanki *et al.* have reported a nickel oxide nanowire-based electrochemical biosensor for the detection of the *Vc* concentration, with a detection range of 37–350 ng mL⁻¹ or 0.44–4.2 nmol L⁻¹.⁴¹ Thus, when compared to the individual metal oxide, the nanohybrid metal oxide/graphene composite is a potential candidate for the fabrication of a biosensor to detect the concentration of *Vc*.

3.10 Specificity, reproducibility and stability tests

The specificity of the immunoelectrode (BSA/Ab-*Vc*/RGO-ant-TiO₂/ITO) was tested against glucose (5 mM), uric acid (5 mM), *Escherichia coli* (300 ng mL⁻¹), *Salmonella typhi* (300 ng mL⁻¹) and *Vibrio cholerae* (300 ng mL⁻¹). This immunoelectrode was incubated (for 5 min) with 15 μ L of these metabolites and pathogens. During these measurements, it was observed that there are no significant changes in the electrochemical response after the addition of the pathogens to the BSA/Ab-*Vc*/RGO-ant-TiO₂/ITO immunoelectrode (Fig. S6[†]). Thus, the specificity of the probe for *Vibrio cholerae* is indicated.

The reproducibility of the results using the immunoelectrode (BSA/Ab-*Vc*/RGO-ant-TiO₂/ITO) was investigated using a concentration of 300 ng mL⁻¹ *Vibrio cholerae* with different electrodes and the changes in the magnitude of the current were observed. It was observed that there was no significant change in the current value, indicating good precision (Fig. S7[†]). The storage stability of the immunoelectrode was monitored by recording its CV curves at time intervals of 10 days for about 50 days (Fig. S8[†]). It was observed that no significant current change occurs for up to 50 days, after which a 5% change in current compared to the original value is observed. Thus, the BSA/Ab-*Vc*/RGO-ant-TiO₂/ITO immunoelectrode reveals excellent storage stability for up to 50 days.

4. Conclusions

We have demonstrated the fabrication of a label-free immunosensor based on a RGO-ant-TiO₂ nanohybrid for the detection of *Vibrio cholerae*. The RGO-ant-TiO₂ nanohybrid platform was utilized for the loading of protein conjugated antibodies specific to *Vibrio cholerae* (Ab-*Vc*). The capacitive properties of this RGO-ant-TiO₂ nanohybrid smart material were explored to detect *Vibrio cholerae* based on its antigen-antibody interactions. Electron microscopy, XRD and UV studies revealed the successful formation of the RGO-ant-TiO₂ nanohybrid material, while FT-IR and electrochemical investigations described its functionalized nature, which made it desirable for antibody attachment. The electrochemical response studies of the BSA/Ab-*Vc*/RGO-ant-TiO₂/ITO immunoelectrode as a function of the

Vibrio cholerae concentration revealed its higher sensitivity, improved lower detection limit (10 ng mL⁻¹ or 0.12 nmol L⁻¹) and long term stability (50 days), arising due to its excellent electrochemical properties and the high electron transfer kinetics of RGO-ant-TiO₂. The results indicate that RGO-ant-TiO₂ is an interesting platform for the immobilization of Ab-*Vc*. The superior sensing (supercapacitive) performance of the RGO-ant-TiO₂ based immunosensor reveals its potential for application in medical diagnostics. This technique provides the opportunity to achieve the effective determination of *Vc* using miniaturized devices based on the RGO-ant-TiO₂ nanohybrid material and could be a better choice for clinical diagnostics.

Acknowledgements

PRS is grateful to the Department of Science and Technology (DST), India for Young Scientist Award and other financial support. Saurabh Srivastava and Md. Azahar Ali thank CSIR for the award of Senior Research Fellowships. PRS thanks to Prof. Subhasis Ghosh, School of Physical Sciences, JNU for allowing me access to AFM studies. PRS also thanks to University Grants Commission (UGC) for award of start-up-grant.

References

- 1 A. P. F. Turner, *Chem. Soc. Rev.*, 2013, **42**, 3184.
- 2 M. A. Ali, S. Srivastava, P. R. Solanki, V. Reddy, V. V. Agrawal, C. Kim, R. John and B. D. Malhotra, *Sci. Rep.*, 2013, **3**, 2661.
- 3 P. R. Solanki, A. Kaushik, V. V. Agrawal and B. D. Malhotra, *NPG Asia Mater.*, 2011, **3**, 17.
- 4 D. Zhai, B. Liu, Y. Shi, L. Pan, Y. Wang, W. Li, R. Zhang and G. Yu, *ACS Nano*, 2013, **7**, 3540.
- 5 N. Gilmartin and R. O'Kennedy, *Enzyme Microb. Technol.*, 2012, **50**, 87.
- 6 P. C. Ray, S. A. Khan, A. K. Singh, D. Senapati and Z. Fan, *Chem. Soc. Rev.*, 2012, **41**, 3193.
- 7 T. Kuila, S. Bose, P. Khanra, A. K. Mishra, N. H. Kim and J. H. Lee, *Biosens. Bioelectron.*, 2011, **26**, 4637.
- 8 P. R. Solanki, M. K. Patel, A. Kaushik, M. Pandey, R. Kotnala and B. Malhotra, *Electroanalysis*, 2011, **23**, 2699.
- 9 Y. Yang, A. M. Asiri, Z. Tang, D. Du and Y. Lin, *Mater. Today*, 2013, **16**, 365.
- 10 Y. C. Chen, X. C. Huang, Y. L. Luo, Y. C. Chang, Y. Z. Hsieh and H. Y. Hsu, *Sci. Technol. Adv. Mater.*, 2013, **14**, 044407.
- 11 V. Biju, *Chem. Soc. Rev.*, 2014, **43**, 744.
- 12 W. Yang, K. R. Ratinac, S. P. Ringer, P. Thordarson, J. J. Gooding and F. Braet, *Angew. Chem., Int. Ed.*, 2010, **49**, 2114.
- 13 Y. Shao, J. Wang, H. Wu, J. Liu, I. A. Aksay and Y. Lin, *Electroanalysis*, 2010, **22**, 1027.
- 14 L. Zhang, Y. Li, L. Zhang, D. W. Li, D. Karpuzov and Y. T. Long, *Int. J. Electrochem. Sci.*, 2011, **6**, 819.
- 15 A. Galal, N. F. Atta and H. K. Hassan, *Int. J. Electrochem. Sci.*, 2012, **7**, 768.
- 16 G. Eda, G. Fanchini and M. Chhowalla, *Nat. Nanotechnol.*, 2008, **3**, 270.

- 17 C. S. Rout, P. D. Joshi, R. V. Kashid, D. S. Joag, M. A. More, A. J. Simbeck, M. Washington, S. K. Nayak and D. J. Late, *Sci. Rep.*, 2013, **3**, 3282.
- 18 A. M. J. Haque, H. Park, D. Sung, S. Jon, S. Y. Choi and K. Kim, *Anal. Chem.*, 2012, **84**, 1871.
- 19 M. Zhou, Y. Zhai and S. Dong, *Anal. Chem.*, 2009, **81**, 5603.
- 20 J. D. Fowler, M. J. Allen, V. C. Tung, Y. Yang, R. B. Kaner and B. H. Weiller, *ACS Nano*, 2009, **3**, 301.
- 21 S. Liu and X. Guo, *NPG Asia Mater.*, 2012, **4**, e23.
- 22 Z. Yin, S. Sun, T. Salim, S. Wu, X. Huang, Q. He, Y. M. Lam and H. Zhang, *ACS Nano*, 2010, **4**, 5263.
- 23 B. Chitara, L. Panchakarla, S. Krupanidhi and C. Rao, *Adv. Mater.*, 2011, **23**, 5419.
- 24 S. Srivastava, V. Kumar, M. A. Ali, P. R. Solanki, A. Srivastava, G. Sumana, P. S. Saxena, A. G. Joshi and B. Malhotra, *Nanoscale*, 2013, **5**, 3043.
- 25 S. Bai and X. Shen, *RSC Adv.*, 2012, **2**, 64.
- 26 P. Wang, Y. Zhai, D. Wang and S. Dong, *Nanoscale*, 2011, **3**, 1640.
- 27 K. Gotoh, T. Kinumoto, E. Fujii, A. Yamamoto, H. Hashimoto, T. Ohkubo, A. Itadani, Y. Kuroda and H. Ishida, *Carbon*, 2011, **49**, 1118.
- 28 S. Guo and S. Dong, *Chem. Soc. Rev.*, 2011, **40**, 2644.
- 29 Z. S. Wu, D. W. Wang, W. Ren, J. Zhao, G. Zhou, F. Li and H. M. Cheng, *Adv. Funct. Mater.*, 2010, **20**, 3595.
- 30 Y. Wang, Z. Li, J. Wang, J. Li and Y. Lin, *Trends Biotechnol.*, 2011, **29**, 205.
- 31 Y. Zou and Y. Wang, *Nanoscale*, 2011, **3**, 2615.
- 32 Z. S. Wu, G. Zhou, L. C. Yin, W. Ren, F. Li and H. M. Cheng, *Nano Energy*, 2012, **1**, 107.
- 33 S. Zhu, J. Guo, J. Dong, Z. Cui, T. Lu, C. Zhu, D. Zhang and J. Ma, *Ultrason. Sonochem.*, 2013, **20**, 872.
- 34 P. Wang, Y. Tang, Z. Dong, Z. Chen and T. T. Lim, *J. Mater. Chem. A*, 2013, **1**, 4718.
- 35 X. Y. Zhang, H. P. Li, X. L. Cui and Y. Lin, *J. Mater. Chem.*, 2010, **20**, 2801.
- 36 J. Shen, M. Shi, B. Yan, H. Ma, N. Li and M. Ye, *Nano Res.*, 2011, **4**, 795.
- 37 J. H. Yun, R. J. Wong, Y. H. Ng, A. Du and R. Amal, *RSC Adv.*, 2012, **2**, 8164.
- 38 S. Palanisamy, S. Cheemalapati and S. M. Chen, *Int. J. Electrochem. Sci.*, 2012, **7**, 8394.
- 39 S. Boujday, A. Bantegnie, E. Briand, P. G. Marnet, M. Salmain and C. M. Pradier, *J. Phys. Chem. B*, 2008, **112**, 6708.
- 40 Q. Li, K. Cheng, W. Weng, P. Du and G. Han, *Microchim. Acta*, 2013, **180**, 1487.
- 41 P. R. Solanki, M. A. Ali, V. V. Agrawal, A. Srivastava, R. Kotnala and B. D. Malhotra, *RSC Adv.*, 2013, **3**, 16060.
- 42 H. Chen, Y. Zheng, J.-H. Jiang, H. L. Wu, G. L. Shen and R. Q. Yu, *Biosens. Bioelectron.*, 2008, **24**, 684.
- 43 V. K. Rao, M. K. Sharma, A. K. Goel, L. Singh and K. Sekhar, *Anal. Sci.*, 2006, **22**, 1207.
- 44 M. S. Chiriaco, E. Primiceri, E. D'Amone, R. E. Ionescu, R. Rinaldi and G. Maruccio, *Lab Chip*, 2011, **11**, 658.
- 45 M. A. Ali, S. Srivastava, P. R. Solanki, V. V. Agrawal, R. John and B. D. Malhotra, *Appl. Phys. Lett.*, 2012, **101**, 084105.
- 46 C. Nethravathi and M. Rajamathi, *Carbon*, 2008, **46**, 1994.
- 47 G. K. Lewis Jr, G. K. Lewis Sr and W. Olbricht, *Meas. Sci. Technol.*, 2008, **19**, 105102.
- 48 E. Barsoukov and J. R. Macdonald, *Impedance Spectroscopy; Theory, Experiment, and Applications*, Wiley Interscience Publications, 2nd edn, 2005.
- 49 P. Bataillard, F. Gardies, N. Jaffrezic-Renault, C. Martelet, B. Colin and B. Mandrand, *Anal. Chem.*, 1988, **60**, 2374.
- 50 I. O. K'Owino and O. A. Sadik, *Electroanalysis*, 2005, **17**, 2101.